# Evolution of dispersion in the melt compounding of a model polymer nanocomposite system

## A multi-scale study

Gaspar, Hugo; Santos, Raquel; Teixeira, Paulo; Hilliou, Loic; Weir, Michael P.; Duif, Chris P.; Bouwman, Wim G.; Parnell, Steven R.; King, Stephen M.; More Authors

**DOI**
10.1016/j.polymertesting.2019.03.013

**Publication date**
2019

**Document Version**
Final published version

**Published in**
Polymer Testing

Polymer Testing 76 (2019) 109–118

Contents lists available at ScienceDirect

Polymer Testing

journal homepage: www.elsevier.com/locate/polytest

Test Method

# Evolution of dispersion in the melt compounding of a model polymer nanocomposite system: A multi-scale study

Hugo Gaspar[a], Raquel Santos[a], Paulo Teixeira[a], Loic Hilliou[a], Michael P. Weir[b], Chris P. Duif[c], Wim G. Bouwman[c], Steven R. Parnell[c], Stephen M. King[d], José A. Covas[a,**], Gabriel Bernardo[a,e,*]

[a] Institute for Polymers and Composites/I3N, University of Minho, 4800-058, Guimarães, Portugal
[b] Department of Physics and Astronomy, The University of Sheffield, Sheffield, S3 7RH, United Kingdom
[c] Faculty of Applied Sciences, Delft University of Technology, Mekelweg 15, 2629 JB, Delft, the Netherlands
[d] ISIS Pulsed Neutron Source, STFC, Rutherford Appleton Laboratory, Harwell Campus, Didcot, OX11 0QX, United Kingdom
[e] LEPABE - Laboratory for Process Engineering, Environment, Biotechnology and Energy, Faculty of Engineering, University of Porto, Rua Dr. Roberto Frias, 4200-465, Porto, Portugal

A B S T R A C T

We investigate the morphological development of polystyrene (PS)-$C_{60}$ nanocomposites along the length of a prototype co-rotating twin-screw extruder with sampling capabilities. The effects of $C_{60}$ concentration and output on the morphological evolution along the extruder are studied employing a suite of characterization techniques covering a wide range of length-scales, thereby shedding new light on the dispersion mechanism in this model system. We show that the relatively new spin-echo small-angle neutron scattering (SESANS) technique is well suited to probe both the distribution and the dispersion of $C_{60}$. SESANS complements optical microscopy (OM) data as it covers sampling areas several orders of magnitude larger than OM. The multi-scale morphological information conveyed by OM, SESANS, SANS and rheological data shows that for larger outputs, $C_{60}$ agglomerates are eroded as they travel along the extruder, resulting in $C_{60}$ dispersion and distribution at both molecular and micrometric levels. The picture is more complex when smaller feed rates are used, as the evolution of $C_{60}$ dispersion depends on the $C_{60}$ loading. For larger $C_{60}$ contents, agglomeration develops along the extruder, whereas dispersion is improved for smaller $C_{60}$ contents. Overall, it is concluded that an over-high feed rate in extrusion does not necessarily result in a bigger size of the nanoparticle agglomerates because of the complex interplay between stresses and residence time.

## 1. Introduction

The incorporation of carbon nanoparticles (CNPs) such as graphene derivatives [1–3], carbon nanotubes [4–7] and fullerenes [8] into polymer matrices [9,10] offers the possibility of substantial improvements in properties – such as mechanical, electrical, thermal and barrier properties – with only very small nanoparticle loadings.

The level of CNP distribution/dispersion has a large impact on the properties of the nanocomposite. Although an homogeneous distribution/dispersion is generally desired (e.g., for mechanical performance), a certain degree of particle agglomeration [11] can also be advantageous (for example, for electrical and thermal conductivities) [12]. Though property improvements have been achieved in a variety of nanocomposites, carbon nanoparticle distribution/dispersion is generally difficult to control, with both thermodynamic and kinetic processes playing significant roles [9,10,12]. In the case of carbon nanotubes and graphene derivatives this task is complicated by the fact that it is usually difficult to precisely control the size and shape of these nanoparticles. Conversely, fullerene $C_{60}$, being a bucky-ball with a diameter of 0.7 nm [13–15], has a very well defined size and shape. For this reason, $C_{60}$ can be used as a model system to help understanding the distribution/dispersion mechanism of carbon nanoparticles: its enthalpic interactions with the polymer matrix are similar to those of carbon nanotubes and graphene and only the entropic interactions (associated with particle sizes and geometries) are different.

In recent years, polystyrene nanocomposites (PSNCs) containing fullerene nanoparticles have been the subject of a number of studies [16–36] reporting improvements in properties such as electrical conductivity [23,24], thermal stability [25–28] and permeability [29,30]. The impact of $C_{60}$ loading and sample preparation conditions on the corresponding degree of distribution/dispersion, glass transition temperature ($T_g$) and melt viscosity have also been the focus of several studies [17,20,35,36].

The miscibility limit of $C_{60}$ in polystyrene, assumed as an absolute and reversible thermodynamic value associated with molecular homogeneity and independent of the pathway followed from agglomerates to

* Corresponding author. Institute for Polymers and Composites/I3N, University of Minho, 4800-058, Guimarães, Portugal.
** Corresponding author.
*E-mail addresses:* jcovas@dep.uminho.pt (J.A. Covas), gbernardo@fe.up.pt (G. Bernardo).

https://doi.org/10.1016/j.polymertesting.2019.03.013
Received 24 October 2018; Received in revised form 10 January 2019; Accepted 10 March 2019
Available online 13 March 2019
0142-9418/ 

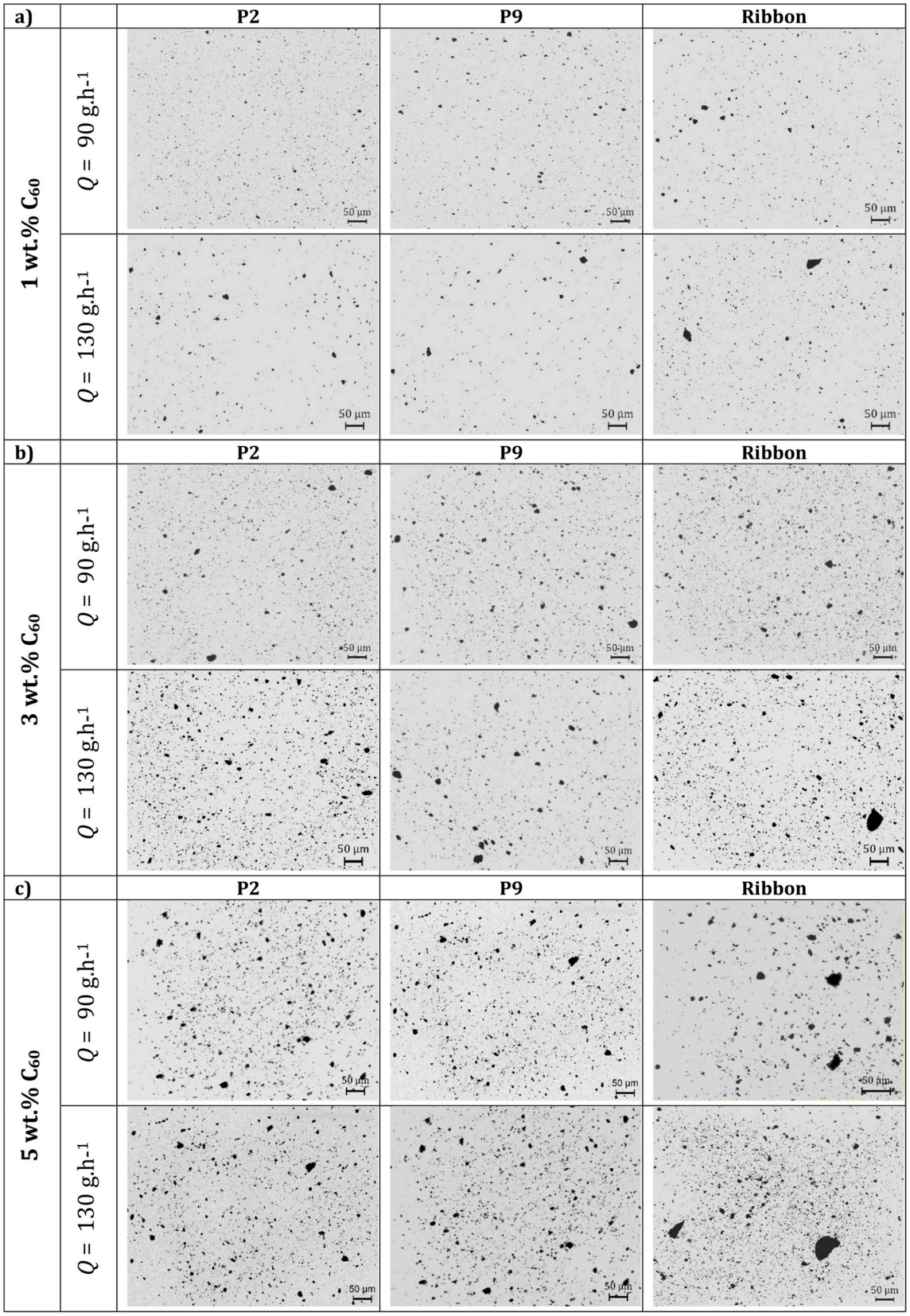


**Fig. 1.** Effect of processing on the degree of dispersion along the extruder.

dispersion at molecular level, was determined by Campbell et al. [22] using wide-angle X-ray scattering (WAXS) as being ~1 wt%. Sanz et al. [35] arrived at the same value using a combination of microscopy, small-angle neutron scattering (SANS) and WAXS experiments. Additionally, these authors determined the dispersibility limit of $C_{60}$ in PS, i.e., the $C_{60}$ loading producing the maximum observed increase in the $T_g$ of the PSNCs as being ~4 wt% $C_{60}$. Loadings beyond this limit gradually reverted the composite $T_g$ towards the neat PS value due to

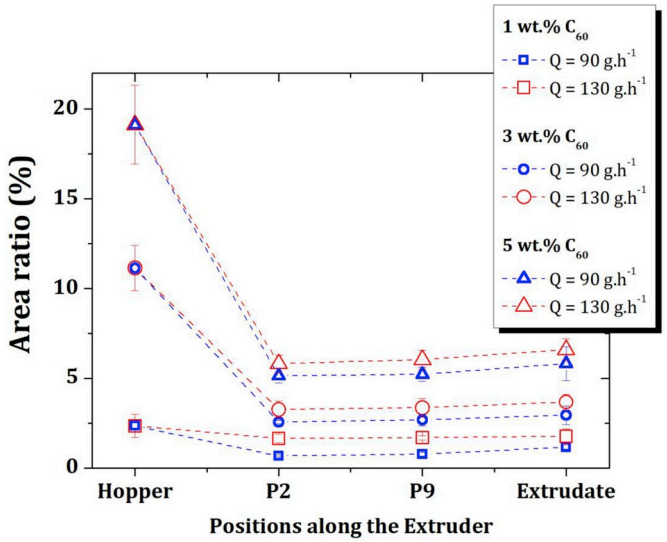


**Fig. 2.** Area ratio evolution along the twin-screw extruder of PS nanocomposites containing 1.0, 3.0 and 5.0 wt% of $C_{60}$.

the occurrence of substantial clustering of $C_{60}$. Similar increases in the $T_g$ of PSNCs with $C_{60}$ loading were also reported by Weng et al. [33] and by Wong et al. [20].

Tuteja et al. [17] studied the impact of $C_{60}$ on the melt viscosity of PSNCs and concluded that a viscosity decrease may occur if the polymer is entangled ($M_w$ = 393 kDa > $M_c$, where $M_c$ is the critical molecular mass for entanglement coupling) and if the average interparticle half-gap ($h$) is less than the polymer size (i.e. $h < R_g$), where $h/a = [\Phi_m/\Phi]^{1/3}$–1, with $\Phi_m$ being the maximum random packing volume fraction (~0.638) and $a$ the particle radius (~0.4 nm). For non-entangled polymer melts ($M_w$ = 19.3 kDa < $M_c$), a viscosity increase was observed upon the addition of $C_{60}$.

In our previous work [36], we studied the impact of feeding conditions (premixed powders of pure components versus a solvent-blended mixture) of $C_{60}$ PSNCs on the dispersion and re-agglomeration phenomena that develop along the axis of a prototype small scale twin-screw extruder. With this device, which allows for the on-line sampling of material at different locations along the barrel without disturbing the extrusion process, we demonstrated that two feeding formulations with widely different initial morphologies converged along the extruder into a similar final nano-morphology. We also described the first application of spin-echo small-angle neutron scattering (SESANS) [37] to the study of this type of multiphase material. SESANS can access optical length scales with neutrons, but in real space (like microscopy) as opposed to reciprocal space (like conventional SANS). It allowed us to demonstrate that SESANS/SANS data can be favourably correlated with OM/TEM images even though SESANS/SANS do not provide the same visually intuitive picture of a sample that OM/TEM do. However, SESANS/SANS are far more sensitive at detecting the phase contrast between carbon and hydrogen-containing compounds and probe a far more spatially-representative volume of the sample than OM/TEM.

In the present study, we extend our previous work to systems of greater industrial relevance by focussing on a single type of feeding formulation (premixed powders of pure components), and explore the effects of feeding rate and nanoparticle concentration on the state of dispersion of $C_{60}$. We note that in our previous work we have only considered one feeding rate and one nanoparticle concentration. Specifically, in the present work we study melt compounding of $C_{60}$ PSNCs prepared using 3 diverse $C_{60}$ loadings (1.0, 3.0 and 5.0 wt%) and 2 different feeding rates (Q). We sample the molten polymer nanocomposite as it travels along the extruder and we characterize the corresponding degrees of dispersion using several techniques covering different length scales from macroscopic to nanoscopic. We place particular emphasis on the complementarity between optical microscopy and spin-echo small-angle neutron scattering (SESANS) [37] characterizations. Additionally, we use SANS to study the dispersion at the nanometer scale. Finally, we characterize the PSNCs using rheometry to obtain an overall understanding of the processing-structure-property relationships in these model systems.

The paper is organized as follows. In Section 2 we describe the sample preparation and characterization methods. In Section 3 we start by characterizing the distribution/dispersion of $C_{60}$ in the PSNC samples using optical microscopy, SESANS and SANS. Next, we measure the

**Table 1**
Dispersion characterization by OM of PS nanocomposites containing 1, 3 and 5 wt % of $C_{60}$ prepared at different feeding rates in a twin-screw extruder.

| | $Q$ = 90 g.h-1 | | | $Q$ = 130 g.h-1 | | |
|---|---|---|---|---|---|---|
| PS nanocomposites with 1 wt % $C_{60}$ | | | | | | |
| Extruder Position | $A_{\chi 75\%}$ (μm$^2$) | $A_{\chi 90\%}$ (μm$^2$) | $N$ (mm$^{-2}$) | $A_{\chi 75\%}$ (μm$^2$) | $A_{\chi 90\%}$ (μm$^2$) | $N$ (mm$^{-2}$) |
| Hopper | 1543.7 | 3361.0 | 169 ± 81 | 1543.7 | 3361.0 | 169 ± 81 |
| P2 | 37.49 | 96.54 | 480 ± 69 | 59.31 | 161.9 | 988 ± 137 |
| P9 | 57.59 | 116.6 | 470 ± 62 | 71.34 | 178.2 | 980 ± 76 |
| Ribbon | 65.90 | 181.1 | 696 ± 71 | 87.43 | 374.5 | 1020 ± 235 |
| **PS nanocomposites with 3 wt % $C_{60}$** | | | | | | |
| Extruder Position | $A_{\chi 75\%}$ (μm$^2$) | $A_{\chi 90\%}$ (μm$^2$) | $N$ (mm$^{-2}$) | $A_{\chi 75\%}$ (μm$^2$) | $A_{\chi 90\%}$ (μm$^2$) | $N$ (mm$^{-2}$) |
| Hopper | 17358.5 | 18838.2 | 132 ± 55 | 17358.5 | 18838.2 | 132 ± 55 |
| P2 | 43.16 | 123.8 | 1700 ± 87 | 54.30 | 145.8 | 1990 ± 369 |
| P9 | 52.87 | 133.8 | 1594 ± 124 | 72.88 | 213.2 | 1768 ± 339 |
| Ribbon | 61.03 | 136.4 | 1704 ± 329 | 90.32 | 472.8 | 1926 ± 341 |
| **PS nanocomposites with 5 wt % $C_{60}$** | | | | | | |
| Extruder Position | $A_{\chi 75\%}$ (μm$^2$) | $A_{\chi 90\%}$ (μm$^2$) | $N$ (mm$^{-2}$) | $A_{\chi 75\%}$ (μm$^2$) | $A_{\chi 90\%}$ (μm$^2$) | $N$ (mm$^{-2}$) |
| Hopper | 34012.2 | 37353.0 | 89 ± 30 | 34012.2 | 37353.0 | 89 ± 30 |
| P2 | 66.75 | 167.3 | 2720 ± 223 | 92.90 | 293.0 | 2722 ± 245 |
| P9 | 91.63 | 198.5 | 2370 ± 291 | 101.9 | 315.8 | 2603 ± 360 |
| Ribbon | 105.6 | 456.9 | 2622 ± 486 | 124.2 | 505.2 | 3006 ± 907 |

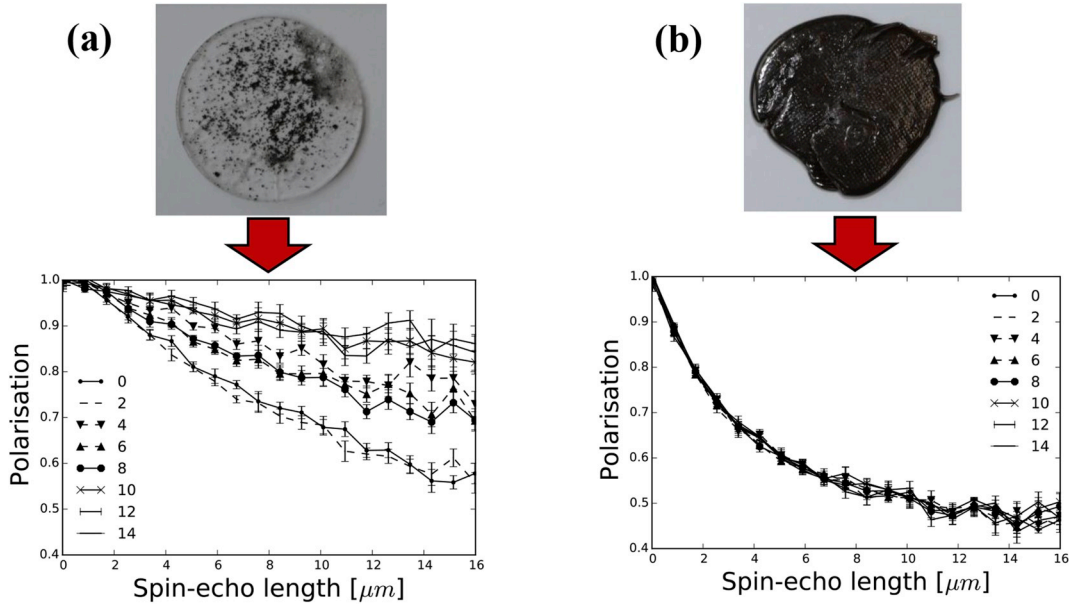


**Fig. 3.** SESANS scans in 2 mm steps across the samples of (a) unprocessed sample with 3.0 wt% $C_{60}$; (b) sample with 5.0 wt% $C_{60}$ collected from P9 (rate = 130 g/h).

rheological response of the samples and we discuss and interpret all the results obtained. Finally, in Section 4 we draw some general conclusions.

## 2. Experimental section

### 2.1. Materials

The $C_{60}$ fullerene was obtained from Solenne BV (> 99.5% purity, $M_w$ = 720.64 g mol$^{-1}$ and density = 1.65 g cm$^{-3}$). The polystyrene was supplied by Sigma-Aldrich (catalog # 430102) with average $M_w$ ~ 192 000, MFI = 6.0–9.0 g/10 min (200 °C/5 kg), and density of 1.05 g cm$^{-3}$ at 25 °C. The polymer $R_g$ is approximately 12 times larger (estimated from $R_g \cong 0.27 M_w^{1/2}$ [38]) than the diameter of $C_{60}$ (~1 nm).

### 2.2. Nanocomposite preparation

The polystyrene pellets were first milled into a fine powder and then pre-mixed with $C_{60}$ powder in the appropriate proportions (1.0 wt%, 3.0 wt% and 5.0 wt%) by vigorously shaking the powder mixture inside a closed container.

The pre-mixes were then melt mixed in a prototype co-rotating intermeshing twin-screw extruder of modular construction, designed to process small amounts of material (in the range of 30–300 g/h, as set by a miniaturized prototype volumetric feeder) but producing the same level of thermomechanical stresses and residence times of larger equipment (Fig. S1(a) in supporting information). Details about this apparatus can be found in the supporting information and elsewhere [36,39,40].

Each pre-mixed powder was compounded at Q = 90 g/h and Q = 130 g/h, with the screws rotating at 80 rpm, in order to create shear rates and residence times representative of the range encountered in larger production machines. Larger Q could not be achieved due to the torque limitation of the motor, whereas smaller Q resulted in unstable extrusion. A flat temperature profile in the barrel and die was kept at 200 °C for all the experiments. In order to assess the quality of the mixing along the extruder, spherically-shaped composite samples in their molten state were collected at positions P2 and P9 (see Fig. S1(b)) during steady state extruder operation, which correspond to screw zones containing kneading disks, where the major changes in morphology/dispersion are likely to occur. These samples were immediately sandwiched between two metal plates covered with Teflon sheets and manually compressed while cooling down and solidifying. With this procedure, the samples were shaped into quasi-circular disks with thickness ~1.5 mm and diameter ~20 mm (see Fig. S2(a) in supporting information). These samples, together with the extruded ribbons (with width ~5 mm and thickness ~ 0.7 mm, as also shown in Fig. S2(a)) collected at the die exit with a minimum draw down to minimize stretching, were then stored for subsequent characterization.

Additionally, some "initial feeding formulation" reference samples were prepared by compression molding the powder pre-mixes, at 170 °C and 10 MPa during 5 min, into flat disks with diameter 25 mm and approximately 1 mm thick (see Fig. S2(b) in supporting information). We note that both SESANS and SANS are sensitive to the presence of air bubbles in a sample and therefore performing SESANS/SANS on a mixture of PS and $C_{60}$ powders (our initial feeding formulation) would produce results with artefacts. Therefore, we had this need to compress the powders into bulk samples deprived of pores.

### 2.3. Nanocomposites characterization

The details of the experimental apparatuses and procedures were previously described [36] and so are not repeated here (see supporting information).

#### 2.3.1. Optical microscopy

The level of dispersion was quantified in terms of the Area ratio (Ar), a widely used index that balances the total area of the agglomerates to the total area analysed, and of the cumulative relative distribution of agglomerates ($C_{C60}$). The latter is determined by summing the areas of the individual agglomerates in ascending area order and dividing by the total area of the agglomerates. In particular, the size of the larger agglomerate contained in 75% (A$\chi$75) and 90% (A$\chi$90) of the total area of agglomerates were followed, together with the number of agglomerates (N) (see Ref. [7] for detail on the definition of these parameters). In these quantifications, only $C_{60}$ agglomerates having circle equivalent diameters higher than 5 μm were used for statistical evaluation, according to the ISO-18553 standard.

#### 2.3.2. Spin-Echo Small Angle Neutron Scattering (SESANS)

Spin-Echo Small Angle Neutron Scattering (SESANS) is a technique

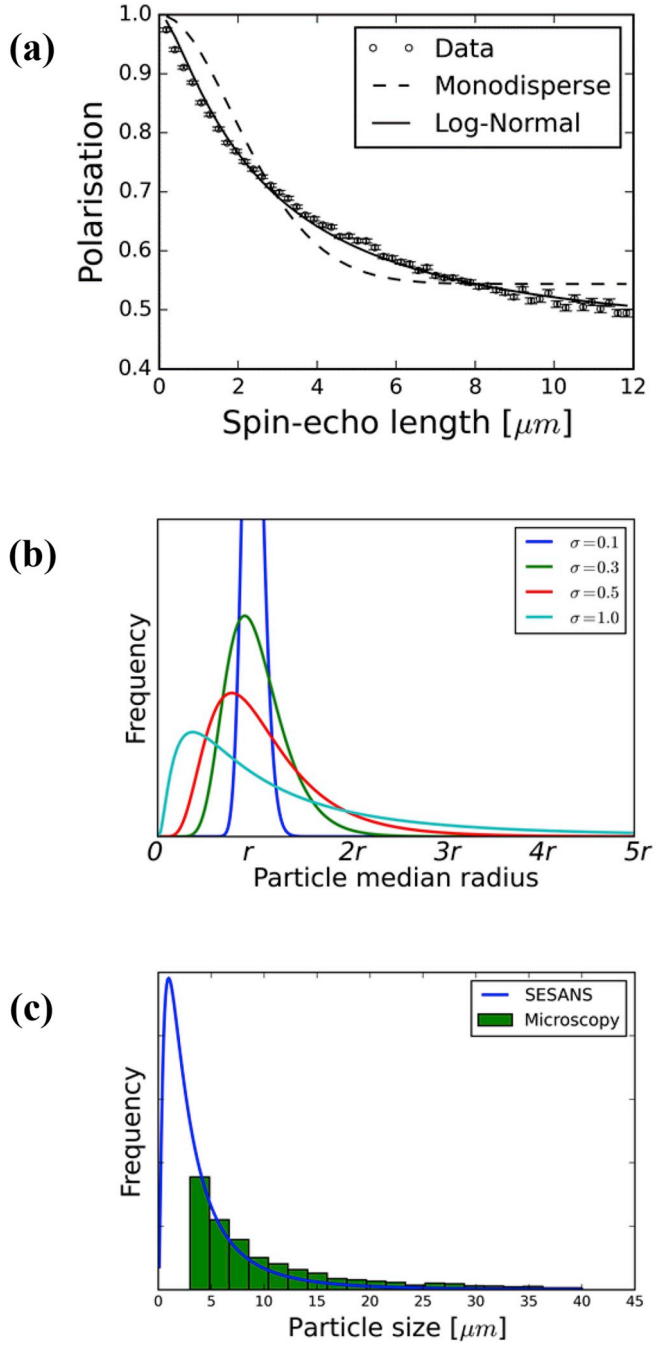


**Fig. 4.** SESANS data analysis: **(a)** Illustration of the effect of including polydispersity in the SESANS model fitting of the 5 wt% $C_{60}$ Q = 130 g/h sample; **(b)** Frequency distribution of the log-normal function for particles of median radius r for various degrees of polydispersity; **(c)** Aggregate size analysis for the 5 wt% sample at 90 g/h. The microscopy data was processed in ImageJ to get the particle sizes and is histogramed from 3 to 40 microns in 2 micron wide bins. The best fit SESANS derived size distribution is scaled for comparison with that from microscopy.

to measure structures of materials. Structures can be determined over three orders of magnitude in length scale, from 10's nm to ~20 μm, the upper bound being two orders of magnitude larger than conventional SANS and comparable to what may be studied with light scattering or OM, though with the complementary benefits afforded by the use of neutrons such as nuclear contrast and bulk sampling [41].

We measured all the samples collected from P9 (a total of 6 samples corresponding to the 3 different concentrations x 2 different feed rates). Additionally, and with the goal of exploring further the potential of this technique in the study of this type of polymer composites, we also measured a compression molded sample of the pre-mixed powder with 3.0 wt% $C_{60}$ (3rd sample from the left in Fig. S2. (b)). As can be seen, since this sample is macroscopically heterogeneous, we performed a scan across the sample using a 2 × 8 mm beam in 8 × 2 mm steps. For comparison, we also carried out a similar scan on a sample with 5.0 wt % $C_{60}$ collected from P9 (rate = 130 g/h). Each of the samples were measured for ~12 h over the same spin-echo length range.

### 2.3.3. Small angle neutron scattering (SANS)

Due to the high carbon to hydrogen ratio in $C_{60}$, there is a naturally high neutron scattering length density contrast with the hydrogenous polystyrene polymer removing the need for isotopic substitution (deuteration). The neutron scattering length densities of hydrogenous PS and of $C_{60}$ are respectively [36], $\rho_N(H\text{-}PS) = 1.41 \times 10^{-6}$ Å$^{-2}$ and $\rho_N(C_{60}) = 5.6 \times 10^{-6}$ Å$^{-2}$ and, therefore, $\Delta\rho_N = 4.19 \times 10^{-6}$ Å$^{-2}$. However, the predominantly hydrogeneous matrix does mean that there is a greater degree of incoherent background scattering that degrades the signal-to-noise, particularly at larger $q$ values.

Samples taken from P2 and P9 were pressed to ~1.5 mm thickness whilst the extruded ribbons were ~0.7 mm thick, but the exact thicknesses of all were measured by a micrometer and those values used in the data reduction procedure to ensure proper scaling.

The fully corrected SANS data were analysed by fitting them to appropriate models using the SasView software (Version 3.1.1) [42].

### 2.3.4. Rheometry

The rheological assessment of the PSNCs was carried out at 200 °C with a stress-controlled rotational rheometer (ARG2, TA Instruments). Disks of the samples collected at P2 and P9 were loaded between the pre-heated parallel plates (diameter 25 mm) and sufficient time was given for thermal stabilization and normal force relaxation (typically 2 min). A time sweep was first performed at 1 Hz with a deformation of 0.1% to confirm the thermal stability and structural equilibrium of all samples within 20 min. Then a new sample was loaded and equilibrated as mentioned above, to record the mechanical spectrum from frequency sweep carried out with a deformation of 0.1%. This deformation was chosen as a result of separate strain sweep experiments performed at 1 Hz to establish the linear viscoelastic regime of the samples.

## 3. Results and discussion

The morphological development, as observed by optical microscopy, of the $C_{60}$ PSNCs containing different loadings of $C_{60}$ and manufactured at the two different rates, is presented in Fig. 1. As clearly shown, the samples contain a large number of microscopic agglomerates whose size and number increases with $C_{60}$ loading. Fig. 2 presents the corresponding progress of the area ratio (total area of agglomerates identified as “dark regions” divided by the total sampling area) along the extruder, and the dispersion characterization results are summarized in Table 1.

In all the samples the area ratio decreases abruptly from the inlet to the sampling port P2, then it remains approximately constant downstream, although a slight tendency for an increase seems to exist within the experimental error. The behavior upstream is as expected and is caused by melting of the polymer together with the high hydrodynamic stress levels associated with flow thorough the kneading block under low temperature [43]. As the temperature of the material progressively increases downstream (in spite of the flat temperature profile, the material temperature is expected to increase progressively along the extruder due to viscous heating and the low thermal conductivity of the polymer melt [44]), the stress level decreases and probably becomes comparable with the magnitude of the cohesive forces binding the $C_{60}$ agglomerates. Moreover, the PSNCs processed at 90 g/h have an area ratio which is systematically lower than that of the PSNCs processed at

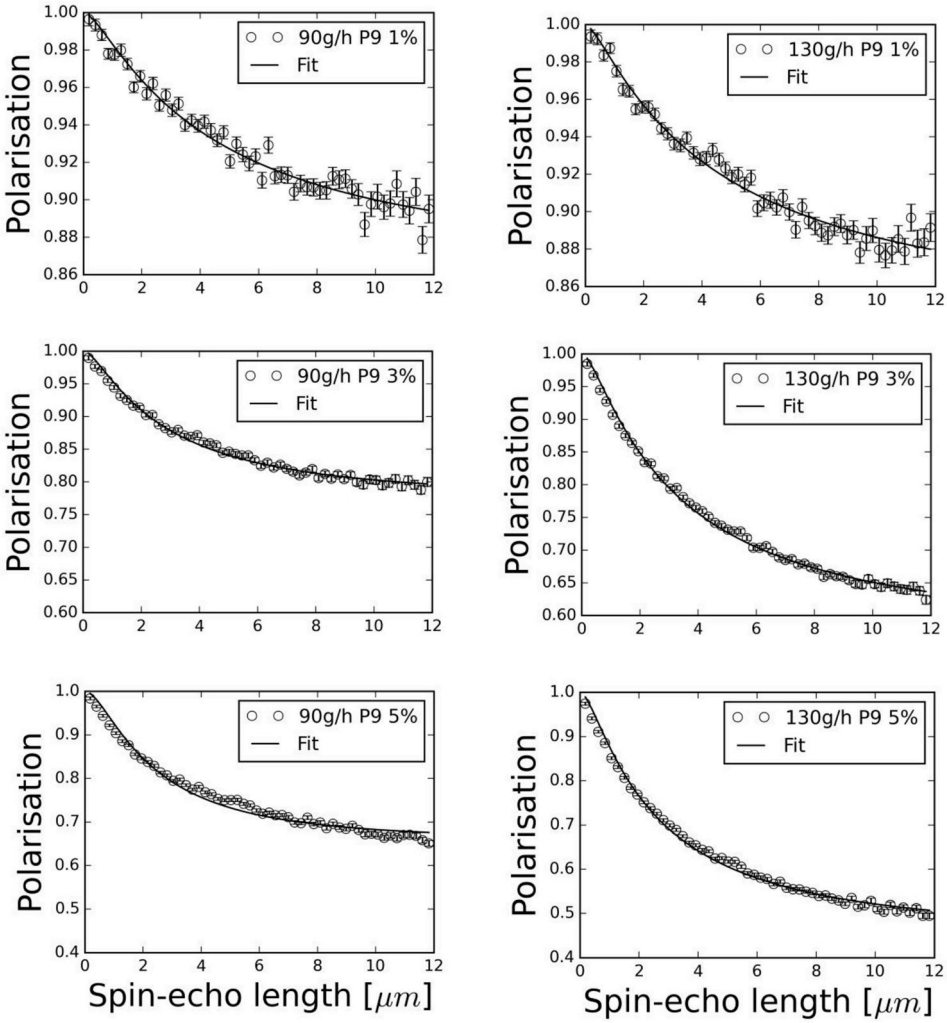


**Fig. 5.** SESANS data from the samples detailed in Table 2 (see legend). Fits incorporating a log-normal polydispersity distribution are shown.

**Table 2**
SESANS fitting parameters derived using a spherical model with a log-normal size distribution, where the radius reported is derived from the median radius. The samples measured were all from position P9. Note that all fits were performed with the SLD constrained to the SANS determined value indicated.

| Wt. % $C_{60}$ | Q (g/h) | Agglomerate Radius (μm) | $10^{-6}$ x Δρ ($Å^{-2}$) | Polydispersity (σ) |
|---|---|---|---|---|
| 1.0 | **90** | 5.9 ± 0.2 | 1.33 | 1.1 ± 0.02 |
| | **130** | 6.62 ± 0.2 | 1.37 | 1.2 ± 0.02 |
| 3.0 | **90** | 3.2 ± 0.08 | 1.37 | 0.97 ± 0.02 |
| | **130** | 5.04 ± 0.08 | 1.63 | 1.1 ± 0.01 |
| 5.0 | **90** | 2.44 ± 0.08 | 1.56 | 0.81 ± 0.05 |
| | **130** | 3.94 ± 0.08 | 1.70 | 1.04 ± 0.01 |

130 g/h. This was also anticipated, since a lower feed rate corresponds to a higher residence time of the material inside the extruder [45], which increases the probability of dispersion. The roles of the hydrodynamic stress and mixing time were studied by Manas-Zloczower et al. [46,47], who defined a fragmentation number as the ratio between the hydrodynamic stress and cohesive strength of an agglomerate, and showed that its magnitude could be correlated with rupture or erosion dispersion mechanisms. Also, they postulated that, at constant stress, the smaller the agglomerate the longer the residence time required to break it. Finally, as observed for other nanofillers, the higher the percentage of incorporation of $C_{60}$, the higher the value of the area ratio.

Fig. 3 shows the SESANS scan results obtained for the compression molded sample of the initial feeding formulation with 3.0 wt% $C_{60}$ and the sample with 5.0 wt% $C_{60}$ processed at 130 g $h^{-1}$ and collected from P9. The effect of extrusion on the dispersion is clear. The unprocessed sample displays spatial inhomogeneity, which produces SESANS signals that vary significantly from region to region, rendering such measurements rather difficult to interpret. By contrast, the 5.0 wt% $C_{60}$ sample collected from P9 produces a SESANS signal that remains approximately constant all over the sample. This set of experiments shows that SESANS is appropriate in probing nanoparticle distribution.

Fig. 4 depicts the SESANS data analysis. In Fig. 4(a) we plot one set of SESANS results obtained for the same sample as in Fig. 3(b), i.e. the sample with 5.0 wt% $C_{60}$ processed at 130 g $h^{-1}$ and collected from P9, and we test fitting the data using a monodisperse dilute sphere model [48] and convoluting a log-normal size distribution. As shown in Fig. 4(a), the quality of the fitting obtained is much better by convoluting a log-normal size distribution. In this distribution the average size ($R_{av}$) is related to the median size (**μ**) and the width of the distribution (**σ**) ($R_{av} = \exp(\boldsymbol{\mu} + \boldsymbol{\sigma}^2/2)$). At this point it is worthwhile to comment on the fact that SESANS data is relatively featureless in certain cases, hence there can be a tendency to over parameterise these curves. Fig. 4(b) represents schematically various parameterisations of a log-normal distribution. As clearly shown, at small sigma ($\sigma = 0.1$) the frequency is close to that of a monodisperse distribution centred at a radius R; however with increasing sigma the distribution is skewed to lower radius with a long distribution out to longer radii. In order to better justify this approach, we have also compared the size distribution

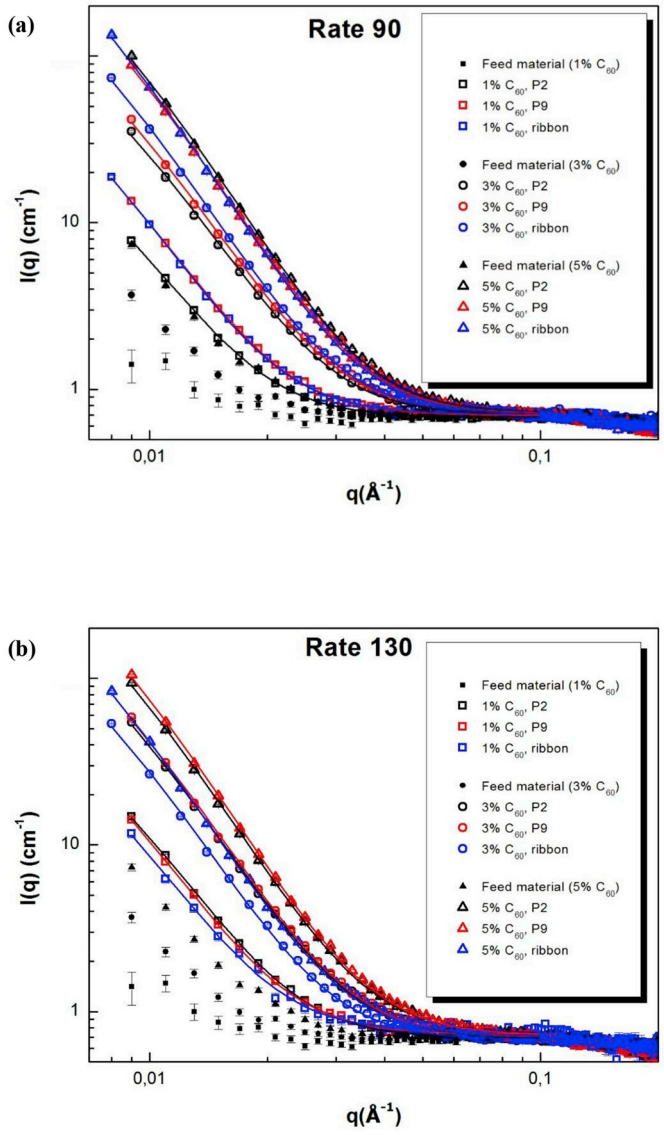


**Fig. 6.** SANS data from the $C_{60}$ PSNCs detailed in Table 3. Discrete data are fitted with the DAB model (lines).

obtained via microscopy with a log-normal distribution parameterised from the SESANS data fits and we have obtained a very good agreement, as shown in Fig. 4(c).

Fig. 5 shows the SESANS results obtained for all the samples collected from sampling port P9 and fitted by convoluting a log-normal size distribution. The fitting values obtained are shown in Table 2 defined by a radius, polydispersity index and contrast value, with the log-normal function parameterised according to the definition given in Thomas [49]. For all samples the scattering length density values used were those determined from the SANS data analysis.

A comparison between the SESANS fitting values in Table 2 and the microscopy area ratio values in Fig. 2 shows that in the case of the PSNCs with 1.0, 3.0 and 5.0 wt% $C_{60}$ there is a very good agreement between both techniques, showing that when the feed rate is 90 g/h the degree of dispersion is higher (smaller area ratio and smaller average size of the agglomerates) than when the rate is 130 g/h. We should however emphasize that in the case of the optical microscopy analysis all the agglomerates having circle equivalent diameters < 5 μm were ignored in the analysis (according to the ISO-18553) and in the case of the PSNCs with 1.0 wt% $C_{60}$ these are statistically very significant. Furthermore, we should mention that in addition to the advantages

**Table 3**
SANS fitting parameters (DAB model) for the $q$ range 0.009–0.1 $Å^{-1}$. $C_{DB}$ is the scaling factor, $\Delta\rho$ is the contrast between the two phases, $L$ is the average distance between the two phases and $m$ is the gradient of the SANS data in the linear region extracted using the power law model ($I(q) \alpha q^{-m}$).

| Wt. % $C_{60}$ | Q (g/h) | Position | Gradient m | Scaling factor $C_{DB}$ ($Å^{-4}$) | $10^6$ x $\Delta\rho$ ($Å^{-2}$) | Correlation Length L (nm) |
|---|---|---|---|---|---|---|
| 1.0 | 90 | P2 | 2.35 ± 0.04 | $1.62 \times 10^{-5}$ | 1.01 | 17.3 ± 0.9 |
| | | P9 | 2.76 ± 0.04 | $2.83 \times 10^{-5}$ | 1.33 | 18.2 ± 0.7 |
| | | Ribbon | 2.76 ± 0.03 | $2.84 \times 10^{-5}$ | 1.33 | 19.5 ± 0.6 |
| | 130 | P2 | 2.70 ± 0.03 | $3.20 \times 10^{-5}$ | 1.42 | 16.2 ± 0.5 |
| | | P9 | 2.69 ± 0.03 | $3.01 \times 10^{-5}$ | 1.37 | 17.7 ± 0.7 |
| | | Ribbon | 2.55 ± 0.09 | $4.83 \times 10^{-5}$ | 1.74 | 17.6 ± 1.8 |
| 3.0 | 90 | P2 | 2.91 ± 0.02 | $7.56 \times 10^{-5}$ | 1.26 | 15.6 ± 0.3 |
| | | P9 | 3.01 ± 0.02 | $8.95 \times 10^{-5}$ | 1.37 | 16.5 ± 0.3 |
| | | Ribbon | 3.16 ± 0.01 | $11.3 \times 10^{-5}$ | 1.54 | 18.9 ± 0.2 |
| | 130 | P2 | 3.12 ± 0.01 | $11.9 \times 10^{-5}$ | 1.58 | 16.7 ± 0.2 |
| | | P9 | 3.14 ± 0.01 | $12.6 \times 10^{-5}$ | 1.63 | 17.1 ± 0.2 |
| | | Ribbon | 3.03 ± 0.01 | $8.2 \times 10^{-5}$ | 1.31 | 17.9 ± 0.2 |
| 5.0 | 90 | P2 | 3.25 ± 0.01 | $21.4 \times 10^{-5}$ | 1.65 | 17.8 ± 0.2 |
| | | P9 | 3.23 ± 0.01 | $19.1 \times 10^{-5}$ | 1.56 | 17.8 ± 0.2 |
| | | Ribbon | 3.28 ± 0.01 | $20.3 \times 10^{-5}$ | 1.60 | 20.4 ± 0.2 |
| | 130 | P2 | 3.23 ± 0.01 | $20.2 \times 10^{-5}$ | 1.60 | 17.4 ± 0.2 |
| | | P9 | 3.28 ± 0.01 | $22.7 \times 10^{-5}$ | 1.70 | 18.2 ± 0.2 |
| | | Ribbon | 3.15 ± 0.01 | $12.7 \times 10^{-5}$ | 1.27 | 19.8 ± 0.3 |

previously mentioned, namely higher phase contrast between carbon and hydrogen-containing compounds and several orders of magnitude larger sampling area, SESANS is a non-invasive technique which is much less time consuming than OM as it does not require any specific sample preparation.

SANS data were used to determine whether extrusion induced any nanoscale orientation of the $C_{60}$ agglomerates in the extruded ribbons. In the supporting information, Figure S3. presents the intensity ratios $I(Q_V)/I(Q_H)$ as a function of $q$ for the vertical and horizontal quadrants of the 2D SANS patterns for extruded ribbons containing 5 wt% $C_{60}$ and processed at the two different rates. As clearly observed, the ratio $I(Q_V)/I(Q_H) \sim 1$, hence it can be concluded that the extrudates are isotropic at the nanoscale. Accordingly, the SANS data were circularly averaged to produce 1D graphs of intensity vs $q$.

Fig. 6(a) displays the SANS data for the samples processed at 90 g/h with different $C_{60}$ loadings and sampled from different positions along the extruder. Also included for comparison are data for the feeding mixtures after being compression molded at 170 °C for 5 min (samples shown in Figure S2(b)). Fig. 6(a) clearly reveals that when the powder mixtures are fed into the extruder an abrupt increase of approximately one order of magnitude in scattering intensity occurs between the inlet and the first mixing zone of the screw. However, the variations in scattering intensity downstream up to the die outlet are much smaller and depend on the $C_{60}$ loading: in the PSNCs with 1% and 3% $C_{60}$ there is a small increase in $I(q)$ along the extruder; in the PSNCs with 5% $C_{60}$ the variation observed is virtually negligible.

Fig. 6(b) shows the corresponding results for the samples processed at 130 g/h. The abrupt increase of about one order of magnitude in $I(q)$ is also observed in the initial part of the extruder, up to P2. Between P2 and the die outlet the variations in $I(q)$ are again much smaller, showing that the variations in nanoscale morphology occur mostly upon melting of the matrix. However, in this case a small decrease in $I(q)$ from P2 to the die outlet is visible. These changes in intensity reflect changes in the size and distribution of the $C_{60}$ agglomerates.

The slopes of the SANS data in their linear regions (between 0.009 and 0.025 $Å^{-1}$) were determined with a simple power law model fit of the form $I(q) \alpha q^{-m}$, where $m$ is related to the fractal dimension of the underlying structure, and the fitting values obtained are presented in Table 3 and in Fig. S4 in the supporting information. While for the rate

of 90 g/h the values of $m$ increase between P2 and the die outlet, for 130 g/h they decrease, these effects being more prominent for the lower $C_{60}$ loadings. More interestingly, when the $C_{60}$ loading increases $m$ increases suggesting, as expected, that the PS-$C_{60}$ interfaces become better defined and the fullerenes become more densely clustered.

The SANS data was fit over its full range using the Debye-Anderson-Brumberger (DAB) model, which calculates the scattering from a randomly distributed two-phase system that is characterized by a single length scale - the correlation length, $L$ - which is a measure of the average spacing between regions of the two different phases (1 and 2). Crucially, this model makes no assumptions about the underlying morphology of the sample. The DAB function has the form:

$$I(\mathrm{q}) = C_{DB}\frac{L^3}{(1+(qL)^2)^2} + background \quad (1)$$

where the pre-factor $C_{DB} = 8\pi K(\Delta\rho)^2\phi_1\phi_2$, where $\Delta\rho$ is the neutron scattering length density difference between the phases having volume fractions of $\phi_1$ and $\phi_2$ and $K$ is a scalar to convert the units of $L^{-1}$ to those of $I(q)$ (i.e. $cm^{-1}$).

As seen in Fig. 6, the DAB model (solid lines) provides a good description of the experimental data. In this case, the data for the "feed material" samples, i.e. samples of mixed powders compression molded at 170 °C (Fig. S2(b) in supporting information) were not fitted because they do not conform to the physics of the DAB model.

The values obtained from the fitting for $C_{DB}$ and $L$ using Equation (1) are shown in Table 3. The values of $\Delta\rho$ calculated from the respective $C_{DB}$ values are also included. All the data are depicted graphically in Fig. S4 in the supporting information. The correlation length shows a systematic tendency to increase in the second part of the extruder, although these changes are relatively small suggesting only minor changes in the quality of the nanodispersion. Therefore, the major changes in the nano-morphology of the $C_{60}$ PSNCs seem to occur in the earlier stages of the process, upon melting of the matrix and flow through the first kneading block.

The full data range was also fitted using a Mass Fractal model [50] (see model description and Fig. S5. in supporting information), which calculates the scattering from fractal-like agglomerates consisting of spherical primary particles of radius $R$, with $R$ assumed to be 3.5 Å (the approximate radius of a $C_{60}$ molecule [13–15]). Very similar characteristic length scales to those obtained using the DAB model were determined (see Table S1 in supporting information).

Rheometry is a useful experimental tool to assess the quality of $C_{60}$ dispersion in PS, as viscoelastic properties are averaged on a macroscopic scale, whereas mechanical spectra are measured in a frequency range able to convey structural information on length scales spanning various order of magnitudes [51]. The mechanical spectra of PSNCs melt processed with the larger feed rate (130 g/h) and collected at P9 are presented in Fig. 7(a). A terminal regime with a Newtonian viscosity at lower frequency is seen in all spectra. Similar results were obtained for all other samples collected along the extruder (see Fig. S6 in supporting information). Thus, within the $C_{60}$ concentration range studied and with the extrusion parameters used, these data indicate that the $C_{60}$ agglomerates do not build a percolated network in the PS matrix. This is expected for low contents of non-interacting hard spherical fillers in a Newtonian matrix, where the zero shear viscosity is described by a reinforcing effect showing a scaling of rheological parameters with the concentration in $C_{60}$ [52,53].

The data plotted in Fig. 7(a) reveals that the mechanical spectra cannot be superimposed on a single master curve, i.e. there is no scaling of the rheological data with the concentration in $C_{60}$. This result is at odds with the mechanical spectra reported for model (truly nano–dispersed) PSNCs studied at volume fractions close to the percolation threshold [51]. The lack of concentration scaling is more evident when rheological parameters such as the zero shear viscosity, $\eta_0$, the relaxation time of the PSNC, $\tau$, the storage modulus measured at low frequency, $G'_{LF}$, and the loss modulus measured at high frequency, $G''_{HF}$ (see the inset of Fig. 7(a) for an illustration on how $\tau$, $G'_{LF}$ and $G''_{HF}$ are determined), are reported as a function of the $C_{60}$ vol fraction. Such representations are illustrated in Fig. 7(b) $\tau$ gives information on the disengagement time of PS chains from the reptation tube (the PS matrix is actually entangled [36]), which is known to be slowed down by topological constraints originating from non-interacting (diluted) nanosized fillers [54]. As such, the increase in $\tau$ shown by the PSNCs with respect to the PS matrix is indicative of some molecular dispersion of $C_{60}$ achieved by melt compounding. The lack of $C_{60}$ concentration scaling of rheological characteristics illustrated in Fig. 7(b) indicates that melt compounding of $C_{60}$ PSNCs performed under similar conditions, but using different $C_{60}$ loadings, generates different states of dispersion. Agglomerates break-up and/or erode during processing of PSNCs leading to the dispersion of single bucky-balls, whilst simultaneously re-agglomeration might occur at locations subjected to lower shear rates, thus impeding recasting rheological data as a single function of $C_{60}$ vol fraction. Effects of matrix reinforcement induced by large $C_{60}$ agglomerates balanced by non-Einstein phenomena caused by molecularly dispersed $C_{60}$ in entangled PS [17,55] could explain the non-monotonic variations.

According to the data in Fig. 7(b), for the largest feed rate tested (130 g/h), all rheological parameters decrease as the PSNCs progress along the extruder (compare the data for samples collected at P2 and P9). This is more evident for $\eta_0$ and $G'_{LF}$ which relate to the macroscopic dynamics of the PSNCs. The acceleration of the PSNC dynamics with increasing residence time in the extruder is less evident when the terminal relaxation time is considered. Note here that the decrease in dynamic moduli and $\eta_0$ cannot be explained by an eventual thermal degradation of PS, as in that case the opposite would occur [36]. Thus, the response of the material could be associated with the dispersion of the $C_{60}$ down to the entanglement mesh size [55–57], in contrast to flow-induced flocculation of fillers which is generally associated with increased viscoelasticity [51]. The agglomerate size reduction along the extruder assessed through rheology is in agreement with the increase in L measured with SANS for the same set of experiments. When the PSNCs are processed using a smaller feed rate, a complex interplay between residence time and filler content takes place. Indeed, the elastic contributions of PSNCs formulated with a volume fraction of $C_{60}$ greater than 1% escalate with residence time (see $\eta_0$ and $G'_{LF}$), confirming the re-agglomeration of $C_{60}$ along the extruder suggested by OM (see Table 1) and by the structural densification pinpointed by SANS (see increase from P2 to P9 in fractal dimension $m$ in Table 3). The opposite effect is seen for volume fractions of $C_{60}$ below 1%, as both $\eta_0$ and $G'_{LF}$ are smaller at P9, indicating that re-agglomeration only occurs when a higher probability for collisions between particles exists, which is effectively realized at larger $C_{60}$ concentration.

## 4. Conclusions

In this work, we investigated the effect of the feeding rate and filler concentration on the degree of $C_{60}$ dispersion in PSNCs along the screw of a co-rotating twin-screw extruder. On the micrometer length scale regime, both OM and SESANS techniques show that the lowest feasible flow rate (Q = 90 g/h) produced composites with a smaller average size of agglomerates. This is a consequence of the increased probability of dispersion due to the higher residence time associated to a lower output.

Rheological data indicates that dispersion of $C_{60}$ down to the molecular scale and some re-agglomeration occurs during compounding, in agreement with the results obtained with the other characterization techniques. However, both feed rate and $C_{60}$ concentration have a complex effect on the morphology evolution along the extruder.

For the feed rate Q = 130 g/h, the rheological data indicates a systematic improvement of $C_{60}$ dispersion from P2 to the die outlet. This result is in agreement with the increase in L (smaller agglomerates mean larger distance between them) and the decrease in $m$ (meaning

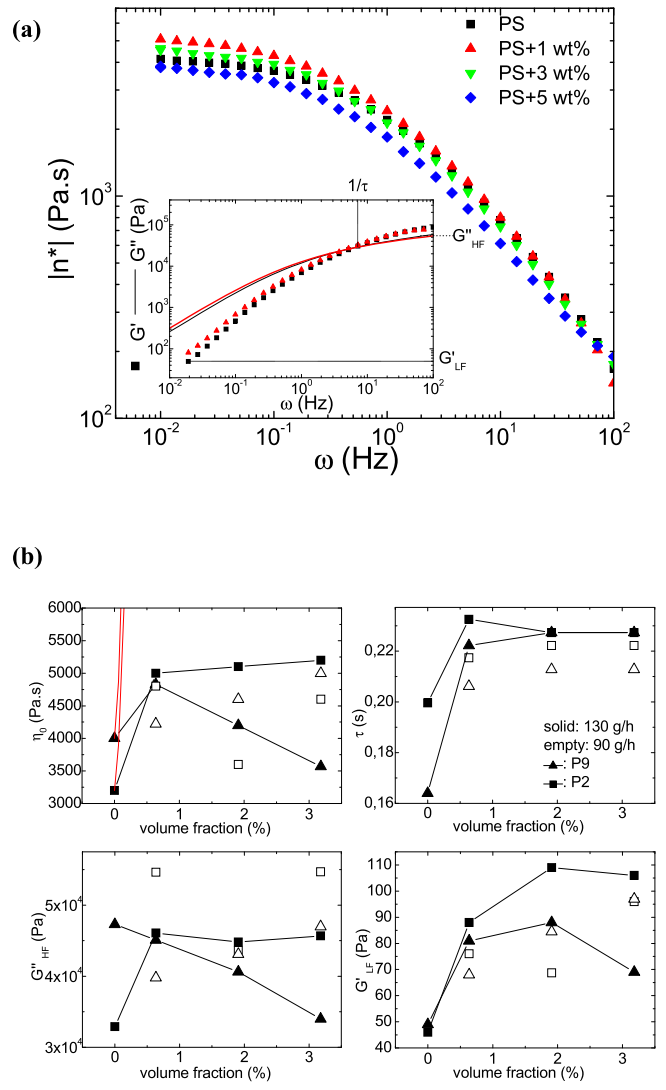


**Fig. 7.** (a) Frequency dependence of the dynamic viscosity $|\eta^*|$ for PSNC with various $C_{60}$ contents (in wt%), collected at P9 and processed with a feed rate of Q = 130 g/h. Inset: frequency dependence of storage G' (symbols) and loss G'' (lines) moduli for the PS matrix (black) and for the 1 wt% PSNC (red) processed and collected under same conditions. (b) $C_{60}$ vol fraction dependence of the zero shear viscosity $\eta_0$, the relaxation time $\tau$, the storage modulus measured at low frequency $G'_{LF}$ and the loss modulus measured at high frequency $G''_{HF}$ for all PSNC samples collected at P2 (squares) and P9 (triangles), and processed under two feed rate conditions (Q = 90 g/h: empty symbols; Q = 130 g/h: filled symbols). Red lines in top left chart are Guth-Gold predictions [52] for PSNC processed with a feed rate of Q = 130 g/h.

more open agglomerates) inferred from SANS data. However, since OM data do not yield such conclusion, particle size reduction seems to be a sub-micron morphological change.

For the feed rate Q = 90 g/h, the situation is more complex, as perceived in the SANS data, because the morphological evolution along the extruder also depends on the $C_{60}$ loading. For larger $C_{60}$ contents, the rheological data suggests a re-agglomeration of $C_{60}$ from P2 downstream, which is in agreement with the increase in agglomerate size and parameter *m* obtained by OM and SANS, respectively. For the smallest $C_{60}$ content studied the trend is opposite as the rheological data suggest an improved $C_{60}$ dispersion along the extruder, thus confirming the overall increase in SANS scattering intensity.

This study provided a valuable example of how SESANS data can be directly related with OM, showing the complementarity between both techniques and emphasizing the main advantages of SESANS as a non-invasive technique, much less time consuming and covering sampling areas several orders of magnitude larger than OM. Therefore, this work opens up the use of SESANS in a technologically important area – polymer nanocomposites – and in the future, we can anticipate a frequent and generalized use of SESANS as a probe of the morphology of these type of systems.

## Acknowledgments

This work was funded by FEDER funds through the COMPETE 2020 Program and National Funds through FCT - Portuguese Foundation for Science and Technology under the project UID/CTM/50025/2013 and grant IF/00606/2014. Funding from FEDER through the program COMPETE (Project EXPL/CTM-POL/0933/2012) is also acknowledged. SANS data were collected during beam time provided through the user program at the ISIS Pulsed Neutron and Muon Source, operated by the UK Science & Tecnology Facilities Council. This work benefited from DANSE software developed under NSF award DMR-0520547. SasView also contains code developed with funding from the European Union's Horizon 2020 research and innovation programme under the SINE2020 project, grant agreement No 654000.

This work was also financially supported by project UID/EQU/00511/2019 - Laboratory for Process Engineering, Environment, Biotechnology and Energy – LEPABE funded by national funds through FCT/MCTES (PIDDAC) and Project "LEPABE-2-ECO-INNOVATION" – NORTE-01-0145-FEDER-000005, funded by Norte Portugal Regional Operational Programme (NORTE 2020), under PORTUGAL 2020 Partnership Agreement, through the European Regional Development Fund.

## Appendix A. Supplementary data

Supplementary data to this article can be found online at https://doi.org/10.1016/j.polymertesting.2019.03.013.

## References

[1] R. Verdejo, et al., Graphene filled polymer nanocomposites, J. Mater. Chem. 21 (10) (2011) 3301–3310.
[2] D. Cai, M. Song, Recent advance in functionalized graphene/polymer nanocomposites, J. Mater. Chem. 20 (37) (2010) 7906–7915.
[3] S.C. Boothroyd, et al., Controlled structure evolution of graphene networks in polymer composites, Chem. Mater. 30 (5) (2018) 1524–1531.
[4] N.G. Sahoo, et al., Polymer nanocomposites based on functionalized carbon nanotubes, Prog. Polym. Sci. 35 (7) (2010) 837–867.
[5] A. Karatrantos, et al., Structure and conformations of polymer/SWCNT nanocomposites, Macromolecules 44 (24) (2011) 9830–9838.
[6] A. Karatrantos, et al., Primitive path network, structure and dynamics of SWCNT/polymer nanocomposites, IOP Conf. Ser. Mater. Sci. Eng. 40 (1) (2012) 012027.
[7] T. McNally, P. Pötschke (Eds.), Polymer–Carbon Nanotube Composites, Woodhead Publishing, 2011.
[8] E. Badamshina, M. Gafurova, Polymeric nanocomposites containing non-covalently bonded fullerene C-60: properties and applications, J. Mater. Chem. 22 (19) (2012) 9427–9438.
[9] S.K. Kumar, et al., 50th anniversary perspective: are polymer nanocomposites practical for applications? Macromolecules 50 (3) (2017) 714–731.
[10] A. Karatrantos, N. Clarke, M. Kröger, Modeling of polymer structure and conformations in polymer nanocomposites from atomistic to mesoscale: a review, Polym. Rev. 56 (3) (2016) 385–428.
[11] D. Walter, Primary particles – agglomerates – aggregates, in: D.F. (DFG) (Ed.), Nanomaterials, 2013.
[12] A.C. Balazs, T. Emrick, T.P. Russell, Nanoparticle polymer composites: where two small worlds meet, Science 314 (5802) (2006) 1107–1110.
[13] K. Hedberg, et al., Bond lengths in free molecules of buckminsterfullerene, C60, from gas-phase electron-diffraction, Science 254 (5030) (1991) 410–412.
[14] C. Gripon, et al., Study of undersaturated C-60 solutions in CS2 by small angle neutron scattering, Fullerene Sci. Technol. 4 (6) (1996) 1195–1211.
[15] Y.B. Melnichenko, et al., Characterization of fullerenes and fullerene derivatives by small-angle neutron scattering and transmission measurements, J. Chem. Phys. 111 (10) (1999) 4724–4728.
[16] M. Mu, et al., Polymer tracer diffusion exhibits a minimum in nanocomposites containing spherical nanoparticles, Macromolecules 44 (2) (2011) 191–193.
[17] A. Tuteja, P.M. Duxbury, M.E. Mackay, Multifunctional nanocomposites with reduced viscosity, Macromolecules 40 (26) (2007) 9427–9434.

[18] J.M. Kropka, V.G. Sakai, P.F. Green, Local polymer dynamics in polymer-C-60 mixtures, Nano Lett. 8 (4) (2008) 1061–1065.
[19] G.G. Vogiatzis, D.N. Theodorou, Local segmental dynamics and stresses in polystyrene-C-60 mixtures, Macromolecules 47 (1) (2014) 387–404.
[20] H.C. Wong, et al., Glass formation and stability of polystyrene-fullerene nanocomposites, J. Mol. Liq. 153 (1) (2010) 79–87.
[21] G. Bernardo, et al., Phase behavior of blends of PCBM with amorphous polymers with different aromaticity, J. Polym. Sci. B Polym. Phys. 54 (10) (2016) 994–1001.
[22] K. Campbell, et al., Role of conformation in pi-pi interactions and polymer/fullerene miscibility, J. Phys. Chem. B 115 (29) (2011) 8989–8995.
[23] L. Perrin, et al., Fullerene-based processable polymers as plausible acceptors in photovoltaic applications, J. Polym. Sci. B Polym. Phys. 51 (4) (2013) 291–302.
[24] C. Chakraborty, S. Malik, J.-M. Guenet, Syndiotactic polystyrene/fullerene composites: elucidation of structural aspect, Polym.Solv.Complexes Intercalates Polysolvat 8 (2011) 303.
[25] B.B. Troitskii, et al., Inhibition of thermo-oxidative degradation of poly(methyl methacrylate) and polystyrene by C60, Eur. Polym. J. 36 (5) (2000) 1073–1084.
[26] E.B. Zeinalov, G. Kossmehl, Fullerene C-60 as an antioxidant for polymers, Polym. Degrad. Stabil. 71 (2) (2001) 197–202.
[27] L. Fernandes, H. Gaspar, G. Bernardo, Inhibition of thermal degradation of polystyrene by C-60 and PCBM: a comparative study, Polym. Test. 40 (2014) 63–69.
[28] P. Pereira, et al., Impact of fullerenes on the thermal stability of melt processed polystyrene and poly(methyl methacrylate) composites, Polym. Test. 47 (2015) 130–136.
[29] A. Higuchi, et al., Preparation and gas permeation of immobilized fullerene membranes, J. Appl. Polym. Sci. 77 (3) (2000) 529–537.
[30] B. Hanson, V. Pryamitsyn, V. Ganesan, Computer simulations of gas diffusion in polystyrene-C-60 fullerene nanocomposites using trajectory extending kinetic Monte Carlo method, J. Phys. Chem. B 116 (1) (2012) 95–103.
[31] J.T. Han, et al., Direct observation of interfacial C-60 cluster formation in polystyrene-C-60 nanocomposite films, Nanotechnology 20 (10) (2009).
[32] O.V. Alekseeva, et al., DSC investigation of the polystyrene films filled with fullerene, J. Therm. Anal. Calorim. 109 (2) (2012) 1033–1038.
[33] D. Weng, et al., The influence of Buckminsterfullerenes and their derivatives on polymer properties, Eur. Polym. J. 35 (5) (1999) 867–878.
[34] R. Dattani, J.T. Cabral, Polymer fullerene solution phase behaviour and film formation pathways, Soft Matter 11 (16) (2015) 3125–3131.
[35] A. Sanz, et al., Influence of C-60 fullerenes on the glass formation of polystyrene, Polymer 68 (2015) 47–56.
[36] H. Gaspar, et al., A journey along the extruder with polystyrene:C60 nanocomposites: convergence of feeding formulations into a similar nanomorphology, Macromolecules 50 (8) (2017) 3301–3312.
[37] M.T. Rekveldt, et al., Spin-echo small angle neutron scattering in Delft, Rev. Sci. Instrum. 76 (3) (2005) 033901.
[38] J.D. Londono, et al., Composition dependence of the interaction parameter in isotopic polymer blends, Macromolecules 27 (10) (1994) 2864–2871.
[39] R.M. Novais, J.A. Covas, M.C. Paiva, The effect of flow type and chemical functionalization on the dispersion of carbon nanofiber agglomerates in polypropylene, Compos. Appl. Sci. Manuf. 43 (6) (2012) 833–841.
[40] A.V. Machado, J.A. Covas, M. van Duin, Evolution of morphology and of chemical conversion along the screw in a corotating twin-screw extruder, J. Appl. Polym. Sci. 71 (1) (1999) 135–141.
[41] M.T. Rekveldt, Novel SANS instrument using neutron spin echo, Nucl. Instrum. Methods Phys. Res. Sect. B Beam Interact. Mater. Atoms 114 (3) (1996) 366–370.
[42] G. Alina, et al., SasView, Date of access: 10/01/2019 Available from http://www.sasview.org/.
[43] J.M. Barbas, A.V. Machado, J.A. Covas, Processing conditions effect on dispersion evolution in a twin-screw extruder: polypropylene-clay nanocomposites, Chem. Eng. Technol. 37 (2) (2014) 257–266.
[44] M.J. Stevens, J.A. Covas, S. Netherlands (Ed.), Extruder Principles and Operation, 1995.
[45] G.R. Kasaliwal, et al., 4 - influence of material and processing parameters on carbon nanotube dispersion in polymer melts, in: T. McNally, P. Pötschke (Eds.), Polymer–Carbon Nanotube Composites, Woodhead Publishing, 2011, pp. 92–132.
[46] A. Scurati, D.L. Feke, I. Manas-Zloczower, Analysis of the kinetics of agglomerate erosion in simple shear flows, Chem. Eng. Sci. 60 (23) (2005) 6564–6573.
[47] N. Domingues, et al., Dynamics of filler size and spatial distribution in a plasticating single screw extruder - modeling and experimental observations, Int. Polym. Process. 25 (3) (2010) 188–198.
[48] R. Andersson, et al., Analysis of spin-echo small-angle neutron scattering measurements, J. Appl. Crystallogr. 41 (5) (2008) 868–885.
[49] J.C. Thomas, The determination of log normal particle size distributions by dynamic light scattering, J. Colloid Interface Sci. 117 (1) (1987) 187–192.
[50] D.F.R. Mildner, P.L. Hall, Small-angle scattering from porous solids with fractal geometry, J. Phys. D Appl. Phys. 19 (8) (1986) 1535–1545.
[51] Y. Song, Q. Zheng, Linear rheology of nanofilled polymers, J. Rheol. 59 (1) (2015) 155–191.
[52] E. Guth, O. Gold, On the hydrodynamical theory of the viscosity of suspensions, Phys. Rev. 53 (1938) 322.
[53] G.K. Batchelor, Effect of Brownian-motion on bulk stress in a suspension of spherical-particles, J. Fluid Mech. 83 (NOV) (1977) 97–117.
[54] R. Mangal, et al., Multiscale dynamics of polymers in particle-rich nanocomposites, Macromolecules 49 (14) (2016) 5202–5212.
[55] A. Tuteja, et al., Effect of ideal, organic nanoparticles on the flow properties of linear polymers: non-Einstein-like behavior, Macromolecules 38 (19) (2005) 8000–8011.
[56] E. Senses, et al., Small particle driven chain disentanglements in polymer nanocomposites, Phys. Rev. Lett. 118 (14) (2017).
[57] A. Karatrantos, et al., Entanglements in polymer nanocomposites containing spherical nanoparticles, Soft Matter 12 (9) (2016) 2567–2574.